PHYSICOCHEMICAL PROPERTIES AND STRUCTURE OF SiC_xN_y:Fe FILMS GROWN FROM A GAS MIXTURE OF FERROCENE, HYDROGEN AND 1,1,3,3,5,5-HEXAMETHYLCYCLOTRISILAZANE

**N. I. Fainer[1], R. V. Pushkarev[1], S. B. Ehrenburg[1],
S. V. Trubina[1], V. A. Shestakov[1], I. S. Merenkov[1],
and M. Terauchi[2]**

Raman spectroscopy, high-resolution transmission electron microscopy (HRTEM), and EXAFS spectroscopy are used to study the composition and structure of SiC_xN_y:Fe films obtained by chemical vapor deposition (CVD) in the Fe–Si–C–N–H system from a mixture of hydrogen, ferrocene $(C_5H_5)_2Fe$, and organosilicon compound 1,1,3,3,5,5–hexamethylcyclotrisilazane (HMCTS) $C_6H_{21}N_3Si_3$. The films are deposited under low pressures (LPCVD) at 1123-1273 K, and their phase composition at 300-1300 K is predicted using thermodynamic modeling. The obtained films are nanocomposites with amorphous matrices containing α-Fe crystallites and carbon clusters with a size of 5-10 nm.

INTRODUCTION

Designing materials possessing a number of various functional properties is a high priority of modern technologies. Spintronics, one of most rapidly developing areas, needs materials with the properties of ferromagnets and semiconductors (or insulators). Successful operation of spintronics devices requires highly efficient injection of spin-polarized current into the semiconductor associated with a minimal polarization loss. The injector is to be a semiconductor with the resistance close to that of the main semiconductor [1, 2] to reduce spin-polarization losses at the injector/semiconductor interface.

Currently, great attention is paid to amorphous ferromagnetic semiconductors [3, 4]. Magnetic and electrophysical characteristics of these materials, including spin-polarized currents inside them, have been studied to a far lesser extent than in their crystalline analogs. The properties of these materials can be controlled and their functional characteristics can be changed widely due to the absence of a long-range order in amorphous substances and different environments of atoms constituting their structure. Besides, electrophysical and magnetic properties can be controlled independently in amorphous semiconductors, which is problematic in the case of crystalline materials where these characteristics are often interdependent [5-7].

Silicon carbonitride is one such example of amorphous semiconductors [8, 9] possessing specific conductivity $\sigma = 10^{-14}$-10^{-6} S/cm, the band gap of 1.5-5.0 eV, and other functional properties which vary widely depending on the structure and composition of the material. Doping silicon carbonitride with iron atoms, which possess the greatest magnetic moment of all transition metals, extends its functional characteristics to create new magnetic materials of various compositions.

The possibility of creating new ferromagnetic materials was demonstrated by a group of researchers who synthesized the four-component ceramics Si–C–N–Fe [10-15]. In our previous studies, we obtained SiC_xN_y:Fe films by high-temperature chemical vapor deposition (CVD) from precursors such as tris(diethylamino)silane (TDEAS), $HSi[N(C_2H_5)_2]_3$ and 1,1,1,3,3,3-hexamethyldisilazane (HMDS), $HNSi_2(CH_3)_6$ in mixtures with ferrocene and helium and showed that these films are composed of silicon carbonitride amorphous matrices with Fe_3Si and $FeSi$ nanocrystals and graphite-like carbon inside [17-19].

In this paper, SiC_xN_y:Fe films were prepared from a gaseous mixture of ferrocene, hydrogen, and a new organosilicon precursor 1,1,3,3,5,5-hexamethylcyclotrisilazane $C_6H_{21}N_3Si_3$ (HMCTS) chosen due to its structure containing a ring as part of its molecule.

THERMODYNAMIC MODELING OF PHASE EQUILIBRIA IN THE Si–C–N–H–Fe SYSTEM

Thermodynamic modeling is widely used to find CVD conditions for obtaining phase complexes or individual phases. It allows monitoring the changes in chemical and phase compositions of the films as functions of the composition, temperature, and pressure of the gaseous mixture. Our modeling implied a quasi-equilibrium CVD regime, i.e. identical compositions of the vapor in the deposition zone and the initial gaseous mixture. The film obtained from the CVD process is a mixture of stoichiometric phases, and the gas phase follows the ideal gas law. Thermodynamic calculations implied the Gibbs free energy minimization for given temperatures and pressures [20]. We used the software and thermodynamic data of the PMM Data Bank (Properties of Microelectronic Materials) created in the NIIC SB RAS for the needs of microelectronics research [21].

When calculating the CVD diagram, it was assumed that the supplied gaseous mixture satisfies the ratio of partial pressures $P[C_6H_{21}N_3Si_3] : P[(C_5H_5)_2Fe] : P[H_2] = 1 : 1 : x$ ($0 \le x \le 50$), the total pressure in the reactor is $P = 10^{-1}$ Torr, and the synthesis temperature is $300 \le T$ (K) ≤ 1300. The modeling was used to study the effect of temperature and hydrogen concentration on the deposition results. The calculations involved 98 molecular forms, including the following 14 condensed phases: Si, Si_3N_4, $FeSi_{2.33}$, $FeSi_2$, FeSi, Fe(α, β, γ), CSi (hexagonal, cubic symmetry), CFe_3, CFe_2, C (hexagonal, cubic symmetry). The calculation results are shown in Fig. 1. $P(H_2)/P(R)$ denotes the ratio of partial pressures of hydrogen and $C_6H_{21}N_3Si_3$, $(C_5H_5)_2Fe$ precursors in the initial gaseous mixture.

As can be seen from Fig. 1, different deposition temperatures can result in six phase complexes of different compositions. Variations of hydrogen concentration, unlike those of temperature, are assumed to have little effect on the phase composition of the film. Note that all phase complexes formed under the above conditions contain carbon. Also, an iron-containing phase complex can be formed.

Each boundary line between the regions of different phase complexes on the CVD diagram can be associated with a reaction of chemical equilibrium determining the position of this line. In particular, the position of the lower boundary line $Si_3N_4 + FeSi_2 + C \mid Si_3N_4 + FeSi + C + Fe$ is determined by the equilibrium $2FeSi_2 + 2N_2 = 2Si_3N_4 + FeSi + Fe$. The next line above $Si_3N_4 + FeSi + C + Fe \mid Si_3N_4 + FeSi + C + Fe_2C$ is determined by the equilibrium $2Fe + C = Fe_2C$. The line $Si_3N_4 + FeSi + C + Fe_2C \mid Si_3N_4 + FeSi + C$ corresponds to the reaction $3Fe_2C + 2Si_3N_4 = 6FeSi + 4N_2 + 3C$. The two remaining lines in the upper part of the figure correspond to the reaction $3C + Si_3N_4 = 3SiC + 2N_2$. Information on the chemical reactions corresponding to the boundary lines can be useful to control the CVD process.

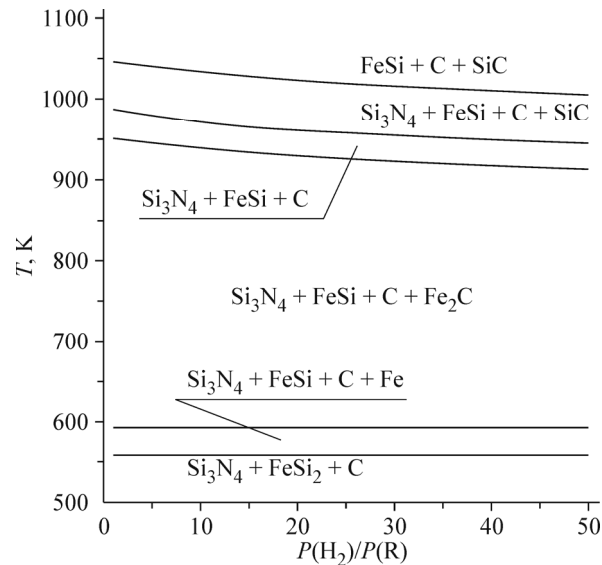**Fig. 1.** CVD diagram of the Fe–Si–C–N–H system for the initial vapor mixture HMCTS+$(C_5H_5)_2$Fe+H_2.

EXPERIMENTAL

The CVD of SiC$_x$N$_y$:Fe films was carried out on silicon substrates Si(100) in a tunnel quartz reactor with the method of high-temperature low-pressure decomposition (LPCVD) of the initial gaseous mixture of 1,1,3,3,5,5-hexamethylcyclotrisilazane cyclic compound, $(CH_3)_6Si_3N_3H_3$ (HMCTS), ferrocene $(C_5H_5)_2$Fe, and hydrogen at 1123-1273 K using an experimental unit described in [22] supplemented by a source of liquid HMCTS and hydrogen used instead of helium. The partial pressures of three gaseous components of the mixture were 10^{-2} Torr for HMCTS, $5 \cdot 10^{-2}$ Torr for hydrogen, and $3 \cdot 10^{-2}$ Torr for ferrocene to make the total pressure of $9 \cdot 10^{-2}$ Torr. The films were prepared on silicon substrates Si(100) after a standard chemical treatment to remove the oxide layer and surface contaminations [23]. The thickness of the films varied from 600 nm to 1 μm, depending on the experiment conditions.

Methods. Chemical composition and chemical bonding of the films were studied with IR, Raman, and energy-dispersive X-ray (EDX) spectroscopies using, respectively, FTIR Shimadzu 8300 spectrometer (300-6000 cm^{-1}, resolution 2 cm^{-1}), PHILIPS PU-95 and Triplemate Spex spectrometers, and a EX-23000BU module for the JSM-6700F scanning electron microscope.

The microstructure of SiC$_x$N$_y$:Fe film surface was studied by scanning electron microscopy (SEM) on a JEOL JSM-6700F microscope with a resolution of 1 nm, and the structure of film deposited at 1273 K was studied on a JEOL JEM-2010 FEF transmission electron microscope with accelerating voltage of 100 kV.

The microstructure of a SiC$_x$N$_y$:Fe sample synthesized at 1273 K was studied using absorption EXAFS spectra (Extended X-ray Absorption Fine Structure) recorded on the BM20, ESRF station, Grenoble, France. The substrate with a film was placed under a beam of monochromatic synchrotron radiation at an angle of ~2-3°. FeK edge absorption spectra were recorded in the energy range of 6867-8091 eV which corresponds to the k-interval up to 16 Å^{-1} (the energy of Fe K-edge is 7112 eV). The spectra were recorded on a 12-channel fluorescence Ge detector. Si(111) was used as a monochromator crystal. Two mirrors with Rh coating were used to focus the beam in horizontal and vertical planes. The X-ray flux during spectra recording was ~$5 \cdot 10^{10}$ photon/s in a 200 μm×5 mm beam. The characterization of the sample was carried out by averaging three spectra obtained. A standard sample of iron foil was measured in the transmission mode, with simultaneous recording of fluorescence spectra of the film.

RESULTS AND DISCUSSION

Films of complex composition SiC_xN_y:Fe were synthesized by thermally decomposing the initial vapor mixture of ferrocene, hydrogen, and HMCTS under a low total pressure of $9 \cdot 10^{-2}$ Torr at 1123-1273 K to study their structure and physicochemical properties. Initially, like in earlier works [17-19], the temperature interval 1073-1273 K was used for the synthesis, but it was discovered in the course of the study that thermal decomposition of HMCTS vapor starts at a higher temperature (1123 K) than that of HMDS and TDEAS.

Elemental composition of SiC_xN_y:Fe films. Fig. 2 shows temperature dependences of atomic concentrations of iron, silicon, nitrogen, and carbon determined by EDXS. The concentrations change nonmonotonically when passing from 1123 K to 1173 K. This sharp change is associated with decomposition of HMCTS vapor at 1173 K. The films obtained at this temperature consist mainly of the products of ferrocene decomposition and, therefore, demonstrate the highest concentration of iron equal to 13 at.%. At higher temperatures of 1173-1273 K, the concentration of iron grows from 3 at.% to 8 at.%, and that of carbon decreases from 57 at.% to 45.5 at.%. The changes of silicon (14 at.%) and nitrogen (22-24 at.%) concentrations in this interval are within the EDXS measurement error. The oxygen concentration is ~1 at.% in all samples.

The concentration of carbon in all samples of this row is lower than in similar films obtained from vapor mixtures (TDEAS)+$Fe(C_5H_5)_2$+He or (HMDS)+$Fe(C_5H_5)_2$+He [17-19] due to lower carbon concentration in the initial compound HMCTS (32.9 at.%) as compared to HMDS (44.7 at.%) and TDEAS (58.8 at.%) and due to the use of hydrogen rather than helium.

Fig. 3 shows IR spectra of SiC_xN_y:Fe samples normalized to the thickness of the films. At 1173-1273 K, they contain the same broad absorption band at 550-1250 cm^{-1} which can be assigned to the superposition of Si–C (800 cm^{-1}) and Si–N (950 cm^{-1}) stretching vibrations. These IR spectra belong to the same range of wave numbers as the spectra typical of silicon carbonitride [24-27]. No hydrogen-containing bonds appear in SiC_xN_y:Fe films.

SiC_xN_y:Fe films were studied by back-scattering Raman spectroscopy on an argon laser (13 mW power) with a wavelength of 488 nm. As was shown in our previous work, silicon carbonitride as such does not exhibit peaks in its Raman spectra [23]. A unique feature of organosilicon layers is that they always contain some free carbon formed spontaneously during the deposition. These clusters of free carbon affect greatly the properties of silicon carbonitride layers. As an example, the conductivity of these layers depends strongly on the concentration of carbon clusters [28], high-temperature thermal stability also results from the presence of free carbon [29]. Formation of free carbon is often observed but, unfortunately, it is not characterized quantitatively. High-resolution electron microscopy and electron diffraction do not allow observing the excess free carbon phase, since:
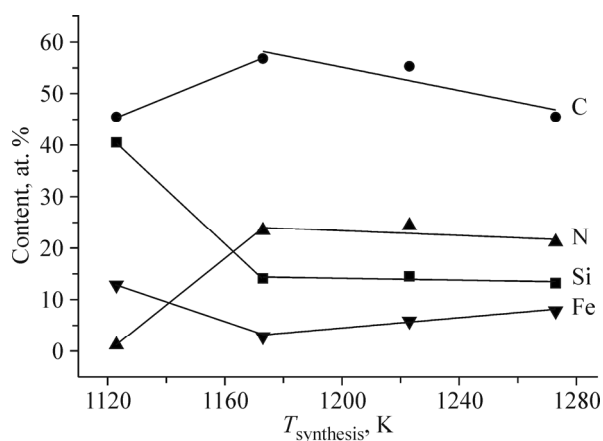

Fig. 2. Atomic content of elements in SiC_xN_y:Fe films as a function of the synthesis temperature.

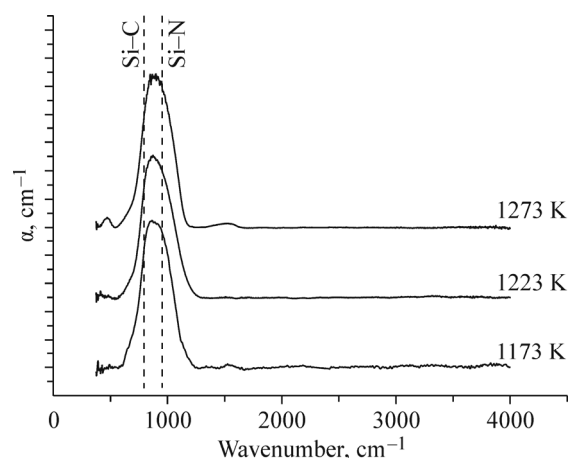**Fig. 3.** IR spectra of SiC_xN_y:Fe films prepared from a gaseous mixture of HMCTS, ferrocene, and hydrogen at 1173 K, 1223 K, and 1273 K.

(1) – the carbon phase is not well-ordered (amorphous) and, therefore, the projections of its potential are similar to those of the amorphous matrix SiC_xN_y to surround carbon nanoclusters;

(2) – the size of ordered carbon regions is much smaller than the thickness (10-20 nm) of the foil exposed to the electron beam. Therefore, well-ordered graphite inclusions will not necessarily be seen on HRTEM images, since these small regions are encompassed by a 10-20 times thicker amorphous matrix [30-32].

In fact, the obtained Raman spectra indicate that carbon regions in the samples are only a few nanometers in size. The shape of Raman spectra and the absence of D and G peaks on the scale of wave numbers for the film obtained at 1123 K testifies no free carbon admixtures. There are only LO and 2LO spectra at 512 cm^{-1} and ~900 cm^{-1} corresponding to the silicon substrate Si(100). All films synthesized at 1173-1273 K have a peak with the highest intensity of the D mode at ~1350-1362 cm^{-1} and a peak with the lowest intensity of the G mode at ~1540-1550 cm^{-1}. It can be assumed in this case that, in spite of the presence of hydrogen in the initial vapor mixture, carbon-containing clusters appear in the form of impurities in SiC_xN_y:Fe films (Fig. 4).

HRTEM images of the SiC_xN_y:Fe film deposited at 1273 K indicate that it is a nanocomposite containing nanocrystals with a characteristic size of 5-10 nm in its amorphous matrix (Fig. 5a). According to the selected area electron diffraction (SAED) data, these nanocrystals refer to the α-Fe phase [33]. The electron micrograph of the local area of the film

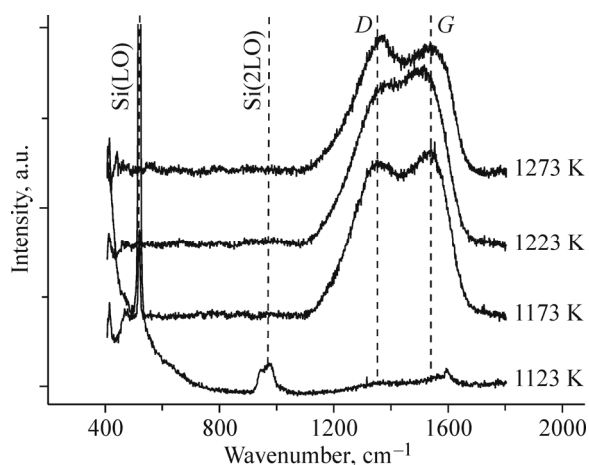**Fig. 4.** Raman spectra of SiC_xN_y:Fe films for various synthesis temperatures in the temperature range of 1123-1273 K.
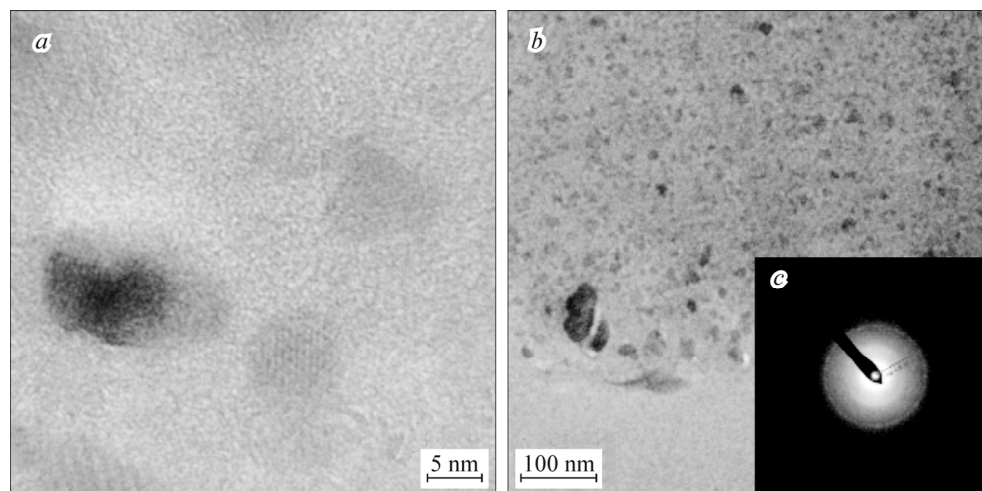

Fig. 5. Different magnifications of cross-sectional HRTEM images of a SiC_xN_y:Fe film prepared at 1273 K (*a*, *b*) and a SAED image (*c*).

1592

consists of a halo and low-intensity diffraction rings to indicate amorphous and crystalline phases, namely, nanocrystals with $d_{hkl} = 2.04$ Å (Fig. 5c) which is quite close to the interplanar distance (110) in α-Fe (2.02 Å). The size of nanocrystals in the structure of the film/substrate interface is much larger and reaches 100 nm. Such difference may be due to a specific interaction involving only iron atoms of ferrocene and silicon atoms of the substrate. In particular, it may be due to the formation of the α-$FeSi_2$ phase at the substrate/film interface characteristic of such deposition processes [18, 34].

A distinctive feature of SiC_xN_y:Fe films obtained in this study as compared to the films described in previous works [17-19] is the fact that they contain iron in the elementary form. In the films deposited using TDEAS and HMDS, the main iron-containing phases are iron silicides FeSi and Fe_3Si. Such a difference in the phase composition of the films is probably related to the structure of the organosilicon precursor used in this work, namely, to the strength of bonds in the ring molecule and, as a consequence, a smaller amount of silicon capable to react with iron. Also, these films contain carbon clusters detected by Raman spectroscopy.

Fig. 6 shows experimental FeK edge EXAFS spectra and their Fourier transform modules (without the account of the phase shift). Simulation of the local environment of Fe atoms was carried out using the EXCURVE 98 program for Fourier filtered data (ΔR 1.6-3.0 Å) with the k^2 weighing and wave vectors varying from 3 Å^{-1} to 12 Å^{-1}.

The parameter $S_0^2 = 0.7$ (amplitude suppression factor due to the many-electron processes) in the calculations was kept constant according to the calculation of the reference compound (Fe foil). During the modeling, the Debye factors of Fe atoms were assumed equal for the first and second (maximum 1 of the radial function) and the third and fourth (maximum 2 of the radial function) spheres, respectively. As can be seen from Fig. 6, the shape (positions of the maxima) of the Fe spectrum of the film is similar to that of metallic iron (the "radial function", Fig. 6, inset clearly images four scattering spheres, like the radial function of the metal). Therefore, for this sample the same model was applied as the one used for metallic iron with the body-centered cubic (BCC) lattice (α-Fe). The total coordination number was taken 14 (as for the metal with the BCC lattice) for the first and second coordination spheres, and 12 for the third and fourth coordination spheres, respectively. The data obtained by modeling the EXAFS spectra are shown in Table 1.

According to the EXAFS data, nanoclusters of metallic iron are formed in the SiC_xN_y:Fe film. This is evidenced by the lack of noticeable amounts of silicon atoms in the environment of iron atoms and decreased interatomic distances in the first and second coordination spheres of iron atoms, which is typical of the structure of nanoclusters. The iron clusters have a somewhat distorted BCC structure, which results in two Fe–Fe distances used in the modeling of the second maximum of
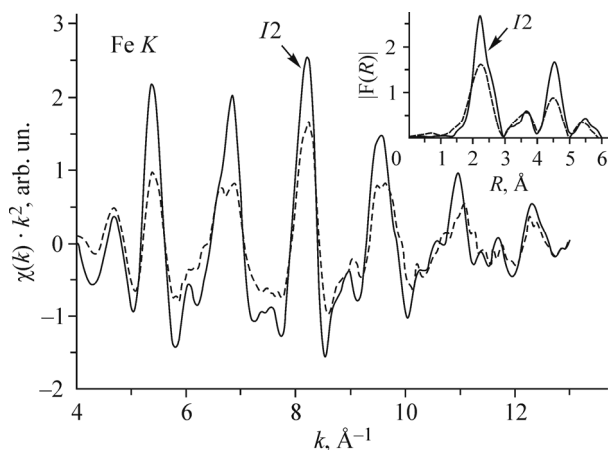

Fig. 6. Experimental FeK-edge EXAFS $k^2\chi(k)$ spectra and their Fourier transform modules ("radial distribution function" without the phase shift) (insert) for the SiC_xN_y:Fe film (dashed line) and a standard sample of iron foil (solid line).

TABLE 1. Parameters of Local Atomic Structures of Fe in SiC$_x$N$_y$:Fe Films and in a Standard Iron Foil

Sample	Absorbing atom–dispersing atom	*N*	*R*, Å	*Fit*
Fe foil	Fe–Fe	**8**	2.481(6)	1.4
	Fe–Fe	**6**	2.857(3)	
	Fe–Fe	**12**	4.07(1)	
SiC$_x$N$_y$:Fe	Fe–Fe	5.7(1)	2.43(1)	1.5
	Fe–Fe	8.3	2.75(1)	
	Fe–Fe	6.2(5)	3.91(1)	
	Fe–Fe	5.8	4.25(1)	

Note. *N* is the coordination number; *R* is the interatomic distance; *Fit* is the factor characterizing the quality of modeling ("fitting"). Fixed parameters are printed bold. The digits in parentheses show the errors of determining the parameters.

the radial distribution function. Thus, according to EXAFS data, no significant number of silicon atoms are bound directly to the iron atoms, since the percentage of formed iron silicides appears to be very small as compared to the content of metallic iron.

CONCLUSIONS

Thermodynamic modeling of chemical deposition of films in the Si–C–N–H–Fe system revealed such phases as Si$_3$N$_4$, FeSi, C, and Fe in the obtained films. However, the predicted phases Fe$_2$C, SiC, FeSi$_2$ were not obtained, probably due to the fact that the system did not reach the equilibrium.

Nanocomposite films SiC$_x$N$_y$:Fe prepared by the LPCVD method from a gaseous mixture of 1,1,3,3,5,5-hexamethylcyclotrisilazane, ferrocene, and hydrogen at a high temperature of 1273 K contain 5-10 nm large iron nanocrystals and 5 nm large carbon nanoclusters inside the amorphous matrix SiC$_x$N$_y$. The structure of the amorphous matrix can be represented as a network of atoms of light elements connected mainly by Si–C and Si–N bonds. The obtained structures are substantially different from previously synthesized SiC$_x$N$_y$:Fe films where iron and silicon formed iron silicides FeSi and Fe$_3$Si. Strong Si–N–Si bonds in the ring fragment of the initial molecule seem to hinder the interaction between silicon and iron atoms to form free crystals α-Fe, and only at the interface between the Si (100) substrate and the SiC$_x$N$_y$:Fe film the interaction is assumed to take place between silicon atoms of the substrate and free iron atoms obtained from ferrocene with the formation of impurity iron silicide α-FeSi$_2$.

REFERENCES

1. V. Sverdlov and S. Selberherr. *Phys. Rep.*, **2015**, *585*, 1.
2. D. D. Awschalom and M. E. Flatté. *Nat. Phys.*, **2007**, *3*, 153.
3. M. J. Mutch, P. M. Lenahan, and S. W. King. *Appl. Phys. Lett.*, **2016**, *109*, 1.
4. W. Liu, H. Zhang, J. A. Shi, et al. *Nat. Commun.*, **2016**, *7*, 13497.
5. A. Gueddim, M. E. Madjet, S. Zerroug, et al. *Opt. Quantum Electron.*, **2016**, *48*, 551.
6. Y. Köseoğlu. *Ceram. Int.*, **2015**, *41*, 11655.

7. D. Saikia and J. P. Borah. *J. Mater. Sci. Mater. Electron.*, **2017**, *28*, 8029.

8. N. I. Fainer, M. L. Kosinova, Y. M. Rumyantsev, et al. *J. Phys. Chem. Solids*, **2008**, *69*, 661.

9. Y. Wang, T. Jiang, L. Zhang, et al. *J. Am. Ceram. Soc.*, **2009**, *92*, 1603.

10. Y. Gou, X. Tong, Q. Zhang, et al. *Ceram. Int.*, **2016**, *42*, 681.

11. Q. Sun, K. Xu, J. W. Y. Lam, et al. *Mater. Sci. Eng. C*, **2001**, *16*, 107.

12. Q. Sun, J. W. Y. Lam, K. Xu, et al. *Chem. Mater.*, **2000**, *12*, 2617.

13. L. Wang, Q. Qi, P. Cai, et al. *Scr. Mater.*, **2017**, *126*, 11.

14. J. Kong, M. Kong, X. Zhang, et al. *ACS Appl. Mater. Interfaces*, **2013**, *5*, 10367.

15. A. Francis, E. Lonescu, C. Fasel, et al. *Inorg. Chem.*, **2009**, *48*, 10078.

16. R. V. Pushkarev, N. I. Fainer, and K. K. Maurya. *J. Struct. Chem.*, **2015**, *56*(6), 1176.

17. R. V. Pushkarev, N. I. Fainer, A. N. Golubenko, et.al. *Glass Phys. Chem*, **2016**, *42*, 490.

18. R. V. Pushkarev, N. I. Fainer, and K. K. Maurya. *Superlattices Microstruct.*, **2017**, *102*, 119.

19. N. I. Fainer, R. V. Pushkarev, V. A. Shestakov, and A. K. Gutakovskii. *J. Struct. Chem.*, **2017**, *58*(8), 1493.

20. A. N. Golubenko, M. L. Kosinova, V. A. Titov, et.al. *Thin Solid Films*, **1997**, *293*, 11.

21. F. A. Kuznetsov, V. A. Titov, A. A. Titov, et al. *Proc. Int. Symp. Adv. Mater.*, **1995**, 24.

22. N. I. Fainer, R. V. Pushkarev, A. N. Golubenko, et al. *Glass Phys. Chem*, **2015**, *41*, 853.

23. N. I. Fainer, A. N. Golubenko, Yu. M. Rumyansev, et al. *Glass Phys. Chem*, **2009**, *35,* 274.

24. N. Fainer, Yu. Rumyantsev, M. Kosinova, et al. *Surf. Coat. Technol.*, **2007**, *201*, 9269.

25. Y. Awad., M. A. El Khakani, C. Aktik, et al. *Surf. Coat. Technol.*, **2009**, *204*, 539.

26. O. Baake, N. I. Fainer, P. Hoffmann, et al. *Nucl. Instrum. Methods Phys. Res.*, *Sect. A*, **2009**, *603*, 174.

27. R. Di. Mundo, F. Palumbo, F. Fracassi, et al. *Plasma Processes Polym.*, **2009**, *6*, 506.

28. Y. Wang, L. Zhang, W. Xu, et. al. *J. Am. Ceram. Soc.*, **2008**, *91*, 3971.

29. T. Varga, A. Navrotsky, J. L. Moats, et.al. *J. Am. Ceram. Soc.*, **2007**, *90*, 3213.

30. S. Trassl, M. Puchinger, E. Rossler, and G. Ziegler. *J. Eur. Ceram. Soc.*, **2003**, *23*, 781.

31. O. Durand-Drouhin, M. Lejeune, M. Clin, and J. Henocque. *Mater. Sci. Semicond. Process.*, **2001**, *4*, 335.

32. R. Kurt, R. Sanjines, A. Karimi, and F. Levy. *Diamond Relat. Mater.*, **2000**, *9*, 566.

33. JCPDS International Center for Diffraction Data.1988. USA. Card no. 6-0696.

34. R. V. Pushkarev, N. I. Fainer, H. Katsui, et al. *Mater. Des.*, **2018**, *137*, 422.